Computationally enhanced quantitative phase microscopy reveals autonomous oscillations in mammalian cell growth

Xili Liu[a], Seungeun Oh[a], Leonid Peshkin[a], and Marc W. Kirschner[a,1]

[a]Department of Systems Biology, Harvard Medical School, Boston, MA 02115

The fine balance of growth and division is a fundamental property of the physiology of cells, and one of the least understood. Its study has been thwarted by difficulties in the accurate measurement of cell size and the even greater challenges of measuring growth of a single cell over time. We address these limitations by demonstrating a computationally enhanced methodology for quantitative phase microscopy for adherent cells, using improved image processing algorithms and automated cell-tracking software. Accuracy has been improved more than twofold and this improvement is sufficient to establish the dynamics of cell growth and adherence to simple growth laws. It is also sufficient to reveal unknown features of cell growth, previously unmeasurable. With these methodological and analytical improvements, in several cell lines we document a remarkable oscillation in growth rate, occurring throughout the cell cycle, coupled to cell division or birth yet independent of cell cycle progression. We expect that further exploration with this advanced tool will provide a better understanding of growth rate regulation in mammalian cells.

quantitative phase | cell growth | single-cell dynamics | periodicity detection

Cell growth is a fundamental physiological property of cells. When cells grow and divide, each component of the cell must double. Although this is well understood for DNA, the strict regulation and coordination of the doubling of all other components is largely a mystery. In nondividing cells, the DNA typically does not double. Yet, under these conditions there is still close control of the level of all other components. Generally, we can say that cell growth, whether balanced or not, is regulated. In proliferating cell populations, it is strictly tied to cell division, resulting in the control of cell size (1, 2). Furthermore, deregulation of cell growth is associated with several diseases (3–6). For a long time, we lacked accurate measurement tools for size of individual cells. Hence, cell growth was measured at the population level, in terms of incremental change in the mean bulk mass or bulk volume, observed in artificially produced synchronous cultures (7, 8). However, there have long been doubts about the effects of drug-induced synchronization on the nuclear mitotic cycle and on the rate of cell mass accumulation (8, 9). Some pharmacological approaches to induce synchrony drive cells from their normal physiological state, for example producing oversized cells, a clear distortion of growth (10). Unsurprisingly, bulk studies led to conflicting conclusions, generating controversy over possible control mechanisms. Several approaches have attempted to circumvent the problem of synchronization of a population of cells by finding ways to extract the average growth rate indirectly in an unperturbed asynchronous population from measurements at a single time point (11–13). Nonetheless, these approaches also make questionable assumptions even though they calculate population averages with high precision. As bulk measures themselves, they cannot address the role of individual variation in cell growth. Therefore, despite the experimental challenges, it has become more and more clear that it is critical to find ways to measure the growth of single cells over time accurately and then convert this information to population averages, if that is desired.

Despite the obvious advantages of single-cell measurements, there are significant experimental challenges. Individual cell growth rate is the change of the mass of a single cell per unit of time, not at a single point in time but at repeated times during the time between divisions. This measurement must be made in live cells without perturbation. It requires extremely accurate size or mass measurement, as the taking of a time derivative greatly amplifies errors. It raises challenges not only in accuracy but also in stability, repeatability, and throughput of the size measurement. Cell growth is a collective description of cell mass or cell volume increase. Although cell mass and volume are generally tightly correlated, it is known that volume change can be transient and decoupled from cell mass at different stages of differentiation or of the cell cycle (10, 14–17). We have therefore focused our analysis on the growth of single-cell mass.

There are relatively few methods that can accurately measure single-cell mass over time in living cells. The suspension microchannel resonator (SMR) is almost certainly the most accurate. It can measure the buoyant mass to a precision of 50 fg or better (18–20), which for a typical cell could be to an error of less than 0.1%. However, its application is limited to cells growing in suspension. At present it cannot be used for cell size measurements of adherent cells over a long time course. Furthermore, in its present form the SMR only allows for the tracking of a few

Significance

It has been a long-standing question in cell growth studies whether the mass of cells grows linearly or exponentially. The two models imply fundamentally distinct mechanisms, and discrimination of the two requires exceptional measurement accuracy. Here, we develop a method, computationally enhanced quantitative phase microscopy, which greatly improves the accuracy and throughput for single-cell growth measurements in adherent mammalian cells. Studies in several cell lines indicate that the growth dynamics of individual cells cannot be explained by either of the simple conventional models; rather, they present an unanticipated and remarkable oscillatory behavior, suggesting more complex regulation and feedbacks in growth, cell division, and size.

cells through an entire cell cycle (20, 21) or many cells for a shorter period of time (22), but not for what is most informative: the tracking of many cells for long periods of time. There are other simpler measurements, all unfortunately based on correlations, such as the use of the nuclear area (23) or assaying a constitutively expressed fluorescent protein (24), as proxies for cell mass. However, these proxies have not been fully verified and almost certainly are not precise enough to make the kinds of critical growth rate measurements that are needed if we wish to reveal small temporal variation in individual cells. In general, correlations between the proxies and cell mass are noisy, reducing confidence in growth rate measurements. Furthermore, for these methods strict proportionality with mass may not hold for all cell types, at different cell cycle stages, or across the full range of the cell mass distribution. For the reasons above, quantitative phase microscopy (QPM) has emerged as the method of choice for accurate dry mass measurements of attached cells down to a precision of less than 10 pg (note it is still more than 100 times less sensitive than the SMR) (18, 25–27). Furthermore, QPM is more readily available, as subtypes of the QPM technique like the quadriwave lateral shearing interferometry (QWLSI) (28), spatial light interference microscopy (29), ptychography (30), and digital holographic microscopy (31) have been commercialized. An especially attractive form of QPM is the QWLSI, which builds the wavefront sensor around an ordinary charge-coupled device (CCD) and can be easily installed onto a conventional microscope. It can be used with the white-light halogen lamp (28), is compatible with fluorescence detection (32), and has the potential for the high throughput and longitudinal applications. However, in our experience, despite the attractiveness of QPM, the highest accuracy can only be achieved with the most optimized yet very restrictive sample configuration and experimental setup. We found that the existing solutions did not provide the stability and robustness required for long-term, large-scale growth rate studies to resolve some of the most pressing issues in the field, such as the debate about the linear or exponential growth in single cells (26). Moreover, single-cell growth trajectories usually are complex, noisy, and have large fluctuations (20, 33–35). One needs to evaluate all of the sources of error carefully to distinguish spurious fluctuations from meaningful regulation. Finally, both an automated image processing and cell tracking pipeline are required to facilitate the high throughput needed to establish the reproducibility of the measurements.

We report here the development of computationally enhanced reference subtraction and image processing methods for QPM (ceQPM), which improve the accuracy of single-cell dry mass and growth measurements. Specifically, we developed a method to generate a reference phase image to remove the phase retardation unrelated to the sample, improved the algorithm of

background leveling, and developed the software for automated image processing, cell segmentation, and cell tracking, all of which enable large-scale longitudinal applications. Using ceQPM, we have more precisely quantified dry mass and growth rate measurements and successfully monitored the growth rate in thousands of cells in each experiment. The results are sensitive enough to reveal a new feature of cell growth, an unexpected autonomous growth rate oscillation coupled to the cell division cycle.

Results

Generating a Reference Phase Image. QPM measures the wavefront retardation induced by a sample. It is quantified as the optical path difference (OPD) relative to a reference wavefront (36). However, the OPD of the optical system is often larger than that induced by the sample. Thus, subtracting the reference OPD is the most critical step of quantitative phase image processing. The reference OPD is generally measured in a cell-free region or from a blank sample. However, this approach is tedious and can be inaccurate in time-lapse imaging because of temporal variation in the system OPD. Here we show the reconstruction of the reference phase image in a more robust manner, which also decreases the noise in measurement.

When light crosses the cell area, its phase shifts due to the refractive index difference between the cell and the medium (Fig. 1). Materials in solution maintain a very strict linear relationship between refractive index and concentration. The slope of that relationship is the specific refractive index increment. For proteins, lipids, carbohydrates, and nucleic acids, the specific refractive index increment, α, falls within a very narrow range, with an average of 0.18 μm^3/pg (37). The OPD for an entire cell is equal to $\int_0^L \alpha \cdot c(h) \cdot dh$, where c is the local cell mass density and L is the cell thickness. Thus, the total cell dry mas can be measured as

$$m = \frac{1}{\alpha} \iint_S OPD(x,y)dxdy,$$

where S is the cell area.

We used a SID4BIO camera (Phasics S.A.) to measure the OPD. The camera is based on QWLSI and optimized for biological applications. It uses a modified Hartmann mask (MHM) to generate four tilted replicas of the wavefront, which form the interferogram on the CCD sensor. A pair of the first-order harmonics $\widetilde{H_x}$ and $\widetilde{H_y}$ in Fourier space carries the information for the spatial gradient of OPD in x and y directions (Fig. 1). Thus, the OPD is calculated as the two-dimensional (2D) integration of the gradients as calculated by the Fourier shift theorem (28, 38, 39). The resultant OPD contains the phase shift
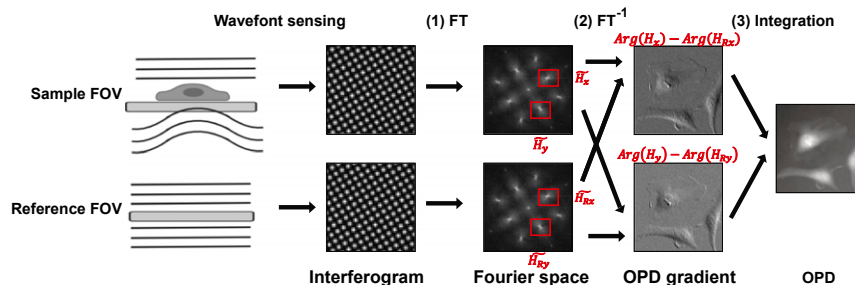
Fig. 1. The principle of QWLSI, showing how a reference wavefront is applied to generate the final OPD of the cells. (1) The interferograms of the sample and reference undergo Fourier Transform (FT). (2) A pair of first-order harmonics in the Fourier space, $\widetilde{H_x}$ and $\widetilde{H_y}$ of the sample image, or $\widetilde{H_{Rx}}$ and $\widetilde{H_{Ry}}$ of the reference image, are selected and undergo inverse Fourier transform (FT^{-1}). The argument of the resultant image is the OPD gradient. Subtracting the reference OPD gradient from the sample gradient of the same direction removes the reference phase shift. (3) The 2D integration of the resultant OPD gradients produces the final OPD image.

Liu et al.

www.manaraa.com

induced by the cell and an additional phase shift due to the aberration of the optical system. A reference wavefront is required to remove the phase shift from the optical system. For the OPD induced by the cell, OPD_{cell}, we have

$$\begin{pmatrix} \dfrac{\partial OPD_{cell}}{\partial x} \\ \dfrac{\partial OPD_{cell}}{\partial y} \end{pmatrix} = \dfrac{p}{2\pi z} \begin{pmatrix} Arg(H_x) - Arg(H_{Rx}) \\ Arg(H_y) - Arg(H_{Ry}) \end{pmatrix},$$

where H_x and H_y are the inverse Fourier-transformed images of the Fourier harmonics of the derivatives along x and y of the sample phase image, while H_{Rx} and H_{Rx} are the corresponding images of the reference, p is the grating period of the MHM, and z is the distance between the MHM and the CCD sensor specific to each camera (28) (Fig. 1).

A blank field of view (FOV) near the sample FOV or an FOV of the same light path on a blank sample is generally used as the reference. However, making a designated blank area in the sample may not always be feasible, and it is tedious and slow to do this manually for large-scale screening. Instead, we have contrived a way to synthesize the reference wavefront. When the confluence of the cells is less than 50%, most of the area of the FOV is blank. Thus, we use the median (and not the mean!) of the sample FOVs as the reference wavefront. As H_x and H_y are in complex number form, we calculate their median by calculating the median of the real parts and the median of the imaginary parts separately:

$$H_{Rx,y} = median\left(real\left(H_{x,y}^{j,j=1,\ldots,N}\right)\right) + i \cdot median\left(imag\left(H_{x,y}^{j,j=1,\ldots,N}\right)\right),$$

where N is the number of sample FOVs. We usually use N larger than 16. When the cell confluence is low and all of the FOVs share the similar light path (e.g., FOVs on a slide or near the center of a 35-mm or larger dish; *SI Appendix*, Fig. S1 *C and D*). This method averages out the noise in the OPD measurement and thus performs better than a single reference image of a blank FOV or a blank sample (*SI Appendix*, Fig. S1*A*). Both the cell confluence and the similarity in the light path affect the quality of the synthetic reference (*SI Appendix*, Fig. S1 *B–D*). For best performance of the method, we usually seed cells at lower than 30% confluency and scan within the central 10% area of a circular dish or well. It is worth mentioning that the rationale for generating the synthetic reference is not limited to QWLSI. The reference light path at any point during a time course can be retrieved through a similar method for other types of QPM. This is especially helpful for QPM systems more subject to reference path distortion due to the use of coherent light sources or long reference arms.

We developed graphical user interfaces (GUI) as well as scripts to generate a position matrix of the desired pattern, make the synthetic reference, and evaluate the performance of the reference image before applying it to the whole dataset. All of these make the high throughput QPM measurements much more convenient and improve the reproducibility and the accuracy of the measurements.

Background Leveling Corrections. As shown in Fig. 2*A*, there is still residual background after compensating for optical system aberration by subtracting the reference image. The residual shape of this background could be due to cover glass thickness variation, vibration, and so on. Background leveling is crucial for accurate dry mass quantification. The conventional methods of polynomial fitting (26) or Zernike polynomial fitting (40) capture the low-frequency background but miss the regional fluctuations (Fig. 2*B*). We developed a method for subtracting both
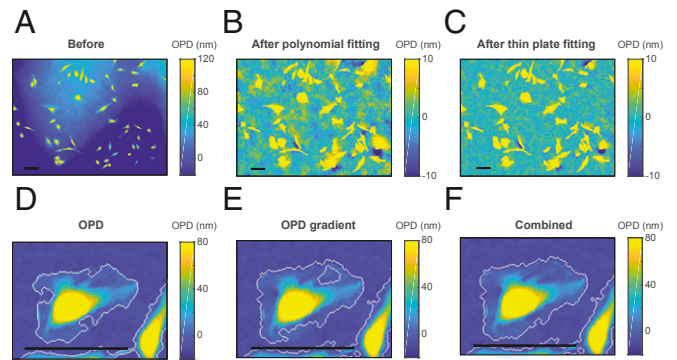
Fig. 2. Background leveling. (*A*) The OPD image before background leveling. (*B*) The OPD image after subtracting the background fitted by a 2D polynomial ($n = 8$). (*C*) The OPD image after subtracting the background fitted by the thin-plate spline. (*D* and *E*) Cell boundaries determined by a threshold on the OPD images (*D*) or the gradient magnitude of the OPD image (*E*). (*F*) The combination of the boundaries on *D* and *E*. *A–C* are from an FOV under a 10× objective lens. *D–F* are from an FOV under 40× objective lens. (Scale bars, 100 μm.)

the low- and high-frequency background, thus significantly improving the precision of the dry mass measurement.

We first isolate the objects from the background by "top-hat filtering." A disk size smaller than most of the cells is chosen as the structuring element to clean up the fluctuations whose scale is comparable to or larger than the cell. The resultant image cannot be directly used for quantification because it subtracts excessive background from the cells, and the mean of the background level varies with each image. We use it only to generate a background mask: We separate the image into the cell and the cell-free areas by combining the filtered OPD image and its gradient magnitude to define the boundary of the cells. Thresholding OPD or OPD gradient alone may leave out part of the cell (Fig. 2 *D* and *E*), but the combination of the two detects the cell boundaries much more accurately (Fig. 2*F*). Note that we intentionally do not fill the holes in either thresholding mask, as other QPM segmentation methods recommend (26, 40), because this process may also fill the blank area within a cell cluster, which is critical for the precise fitting of the cell-dense area. Finally, we create the background image by fitting the cell-free area of the original image with a thin-plate spline method (41). A mesh grid binning is used for fast computation. The thin-plate fitting is parameter-free and can capture both large and small curvatures. Fig. 2*C* shows that our method generates a cleaner background than conventional methods.

The Precision of Dry Mass Measurements. The dry mass measurement error contains all of the variation in the OPD measurement, the background subtraction, and the cell segmentation. Among those factors, the background subtraction has the largest effect, as the unevenness in the background affects the cell boundaries. We quantified the precision of the dry mass measurement by measuring the same fixed cells multiple times at different positions. The result is summarized in Table 1. Our background subtraction algorithm significantly improved the precision of the dry mass measurement. The combined temporal and spatial error is reduced at both high (40×) and low (10×) magnifications when compared to a previous study using a similar setup but different data processing algorithms (table 4 in ref. 26). Remarkably, the error at 10× is reduced by more than twofold from 4.37% in Aknoun et al. (26) to 1.97% in our study. As the magnification decreases from 20× to 10×, the FOV is four times larger, while the measurement error increases only 1.15-fold. We, therefore, gain acquisition throughput at low magnification without sacrificing much precision of measurement. For this reason, we optimized our data collection to maximize throughput at 10×.

Table 1. Dry mass measurement precision at different magnifications

Magnification	OPD noise, nm	FOV area, µm*µm	Temporal error, %	Spatial error, %	Combined temporal and spatial error, %
10×	1.68 (0.21)	1,184*888	1.29 (0.51)	1.54 (0.57)	1.97 (0.86)
20×	1.29 (0.04)	592*444	1.05 (0.37)	1.21 (0.48)	1.71 (0.75)
40×	0.88 (0.16)	296*222	0.57 (0.23)	1.15 (0.46)	1.30 (0.70)

The measurement errors of each cell were quantified as the coefficient of variation (%) of its dry mass measurements. The table lists the mean of the errors quantified in more than 50 cells with the SD of the population in the brackets (see *Materials and Methods* for details). Note that the spatial displacement used in this study corresponds to the big displacement in Aknoun et al. (26).

We also investigated how extracellular matrix (ECM) affects the accuracy of the cell mass quantification. Most of the ECM comes from the fibronectin coating; therefore, we measured the fibronectin level by immunostaining. We found that although the coating is uniform, cytoskeleton remodeling and cell migration rearrange the fibronectin underneath the cell. We estimated that fibronectin contributes 1 to 3 pg to the total cell dry mass, which is not significant compared to the average cell mass of 600 pg. Notably, the variation of fibronectin is even less, than 1 pg in 24 h (*SI Appendix, Quantification of the Extracellular Matrix Contribution of Fibronectin to Cell Dry Mass*).

Cell Segmentation and Cell Tracking. For cell segmentation, the watershed algorithm works the best when a nuclear marker is used as the foreground marker (42). When no nuclear marker is available, we use the local maximum of the cell after top-hat filtering. Because two cells may closely contact each other and form only one local maximum or one cell may have two local maxima, segmentation without any nuclear marker possesses about 5% error depending on cell types. We now find it most useful to combine the OPD image and its gradient magnitude to define the boundary of the cells, as discussed in *Background Leveling Corrections*.

To automatically track cell mass in time, we first identify all of the mitotic cells in the time series based on their rounded morphology, by their mass density gradient and area (Fig. 3A). We then trace cells backward. Each track starts from the end of the time series or a mitotic event. No new track is added during the tracing process. We use cell mass, area, and centroid position as the metrics for tracing. We compare a cell k on frame i with each cell on frame $i-1$ by the weight function:

$$W = d * w_D + |r_m| * w_M + |r_a| * w_A + (j-i+1) * w_G,$$

where d is the distance between the centroids; r_m is the relative mass difference; r_a is the relative area difference; j indicates when the metrics of cell k were last updated; and w_D, w_M, w_A, and w_G are the weights of the respective terms. The dry mass measurement is precise enough that we can have high confidence in the mass term. The weight parameters for HeLa are summarized in *SI Appendix*, Table S1, as an example. The value of W is used to determine the goodness of the match. A good match should have the smallest W on the frame and $W < 1$. When cell k has a good match, its metrics are updated with the newly traced cell. Otherwise, the old metrics are carried on for comparison with the next frame. This method may leave gaps in tracks that can be filled later by a smoothing algorithm but tolerate most of the segmentation error. The track does not terminate or deviate by wrong segmentation of a single frame. A track essentially terminates when it cannot find a good match for more than 10 frames $(j-i+1) * w_G > 1$. In the last step, we trace the lineages of the cells. We compare the metrics at the end of each track with all of the mitotic cells. If a track ends just before a mitotic event (the time axis is inverted), the centroid position is near the position of the mitotic cell, and the mass is close to half of the mitotic mass, the track is identified as the daughter cell of the mitotic cell. Because newborn cells tend to contact their sisters closely, this

will often result in problematic segmentation. For that reason, many cells cannot be traced back to the very beginning of birth. For consistency, we designate the division time (the last frame of mitotic rounding) of the mother cell as the birth time of the daughter cells.

Fig. 3B shows an example of a cell traced to its granddaughter cells (the corresponding OPD images are presented in Fig. 3C and Movie S1). We used the green fluorescent protein (GFP)-fused geminin degron (Geminin-GFP), which begins to accumulate at S phase entry, to report the G1/S transition (43). Specifically, the G1/S transition is defined by the steepest slope of log(Geminin-GFP) accumulation curve in single cells (Fig. 3D). Using the methods described above, we were able to successfully trace the cells in a completely automated fashion without manual supervision or correction. The fraction of mistraced cells identified by manual counterchecking is less than 2%. Movie S2 shows an imaging area of 9.47 mm × 7.99 mm on one well of the six-well plate monitored for 48 h under 10× objective. A total number of 2,983 cells were traced in the area. Six imaging areas of such can be measured within 30 min. The limit of the measurement throughput is the speed at which we can move the stage without perturbing the optical stability of the culture medium surface (see *Materials and Methods* for specification) and the rotation speed of the filter turret.

Evidence for Growth Rate Oscillations during Cell Growth. It has been a long-standing question whether the growth of individual proliferating cells can be described as linear or exponential (7). It is surprisingly difficult to distinguish the two models, because cell size just doubles in one proliferation cycle, rendering the maximum difference between the two models only 5.63% (13, 19). An SMR study revealed complex growth dynamics in suspension cells, in which the growth efficiency is primarily determined by the cell cycle (44). However, the growth regulation in adherent cells may be different from the suspension culture. Since our measurement error is lower than 2%, it allows us to effectively address this question in adherent mammalian cells, monitored throughout the cell cycle. To ensure the highest measurement accuracy, we cleaned up the individual cell growth trajectories by eliminating any data points where the cell was in contact with another cell, as the cell-to-cell contact usually causes erroneous segmentation of more than 2% dry mass. Furthermore, we eliminated rounded cells, as their dry mass error is also larger due to the dramatic change of height and the problem of phase unwrapping (Fig. 3B). In most trajectories, the first 1.5 h after birth and the last 0.5 h before division were removed during this process due to each of these filtering criteria. We found the filtered data implied mass accumulation during mitosis (*SI Appendix*, Fig. S2), which is consistent with the mitotic growth dynamics in suspension cells measured by SMR (21). The filtering process discarded most of the cell trajectories, and fewer than 10% were used in the following analysis. We collected 340 full-cell-cycle trajectories of HeLa cells from three replicate experiments and pooled all of the trajectories together to investigate which model explains the growth dynamics best. We compared the goodness of fit by the small-sample Akaike information criterion (AICc); the better fit possessed the smaller

Liu et al.
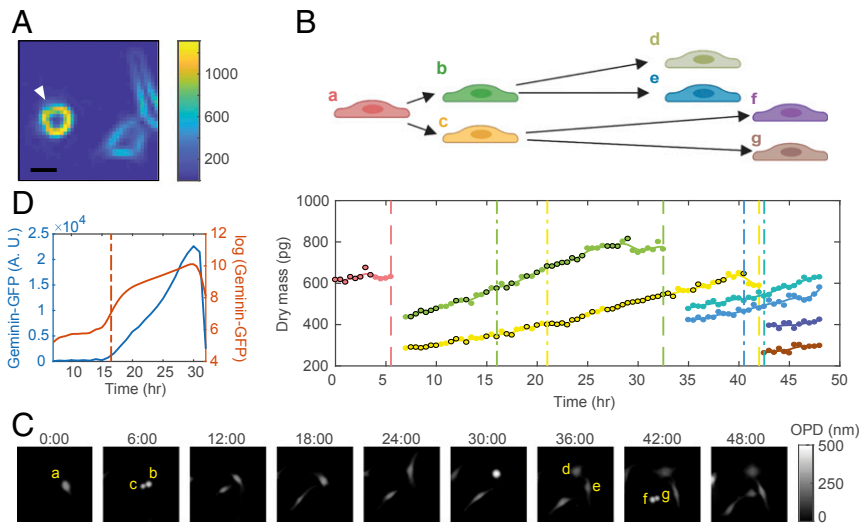
Fig. 3. Cell tracking. (*A*) The gradient magnitude of an OPD image measured at 10×. (Scale bar, 20 μm.) The arrow indicates a mitotic cell. (*B*) One cell is traced to its granddaughter cells. Each color represents a cell. Solid dots are the raw data of dry mass measurement. Dots with black edge indicate data points of cells not in contact with other cells or rounded; dots without black edge indicate date points removed during the filtering process. Solid lines are the spline line smoothing. Vertical dashed lines indicate the timing of cell divisions. Dashed-short dashed lines indicate the timing of G1/S transitions. (*C*) The OPD images of the representative cells in *B* at each sixth hour. (Scale bar, 50 μm.) a–g indicate the corresponding cells in (*B*). (*D*) The intensity of Geminin-GFP measured in one cell (blue) and its logarithm (red). Dashed-short dashed line indicates the steepest slope of the log(Geminin-GFP) accumulation curve, which is defined as the time of the G1/S transition.

AICc (45) (*SI Appendix, The Goodness of Fit of the Linear and Exponential Growth Model*). The mean mass of the whole population increases with time except for a small dip in the last 0.5 h before division (Fig. 4*A*). The dip may have been partially due to a loss of large cells in the mean trajectory during mitosis, as large rounded cells were more likely to be eliminated in the filtering process (*SI Appendix*, Fig. S3 *A* and *B*). However, the cells traced to the end of the cell cycle still showed a 0.5% mass drop in the last 0.5 h (*SI Appendix*, Fig. S3*B*). The timing and magnitude of the dip are consistent with the drastic slowdown or even negative growth before the metaphase-to-anaphase transition, previously noted for mammalian cells in suspension culture (21). The similar quantitative pause of growth in our attached cells and in suspension cells further confirms the measurement accuracy obtained with ceQPM and suggests a universal growth pause just before the metaphase-to-anaphase transition. The exponential model fits the mean mass trajectory before the dip much better than the linear model (Fig. 4*A*, ΔAICc = 102.97), which is consistent with the positive correlation between growth rate and cell size found previously (34). Yet, neither model fits every cell. The exponential model fits better in 68.6% of the population, whereas the linear model fits better for the rest (Fig. 4*B*). The ratio was similar in another adherent cell line, RPE1 cells, where 61.5% cells were fit better by the exponential model (*SI Appendix*, Fig. S3*C*).

The observed growth dynamics were definitely more complex than either of these simplified models. We found the residual of the fit in some single-cell trajectories seemed to be oscillatory, which was particularly intriguing (*SI Appendix, Fig. S3D*). The oscillatory behavior is the most apparent in the mean of the growth rate trajectories aligned to cell division time (Fig. 4*E*). In our initial analysis, we smoothed the mass trajectories and took their time derivative by fitting the linear slope in a short sliding time window. These manipulations of the data should not change the overall shape, exponential or linear, but the smoothing and derivative have the potential to generate an artifactual appearance of periodicity in nonperiodic data (*SI Appendix, The Effect of Data Processing on the Data Power Spectrum*).

To investigate the unexpected growth rate oscillation, we therefore went back to the original unsmoothed raw dry mass data and asked if these unprocessed data were periodic. Proof for periodicity in noisy observations has been thoroughly considered in astronomy as well as in biology (47–49). It is most important to formulate the problem of "whether periodicity exists" as a statistical question and test it against a null hypothesis model of random fluctuation. To ask this question in our raw ceQPM data, we employed the robust detection method developed by Ahdesmäki et al. (46). It derives the "robust" periodogram from a correlogram spectral estimator and tests the significance of the maximum peak against the null hypothesis of randomly permutated data. This method has special advantages as it is insensitive to outliers, applies to short time series, and does not require assumptions on the form of noise. Similar to Fisher's g-test (50), this method defines the g-statistic as

$$g = \frac{max_{1 \leq l \leq 2N-1} S(f_l)}{\sum_{l=1}^{2N-1} S(f_l)},$$

where $S(f_l)$ is the spectral estimation at the frequency f_l, with $f_l = \frac{l \cdot f_s}{2N}$, $l = 0,1, \ldots, (2N-1)/2$, N is the length of the trajectory, and f_s is the data acquisition frequency. f_c denotes the frequency at the maximum of $S(f_l)$. If the trajectory is determined to be oscillatory, f_c equals the oscillation frequency. The P value of the observed g-statistic was estimated by 5,000 randomly permutated trajectories. It allowed us not only to investigate the dominant 5-h period oscillation, which we found in the average growth rate trajectory, but also to discover oscillations of any frequency and amplitude if they were more significant than noise. We first detrended individual dry mass trajectories by the second-order polynomial, which fits better than either the exponential or linear models in 63.9% cells (*SI Appendix*, Fig. S3*F*). We next aligned those trajectories to the time of cell division and averaged them (*SI Appendix*, Fig. S3*G*). The periodogram of the mean trajectory presented two distinct peaks (Fig. 4*F*). The peak at 0.053/h (19.0-h period) could be due to the imperfect detrending or actual growth rate slowdown in the middle of cell cycle. As

Liu et al.
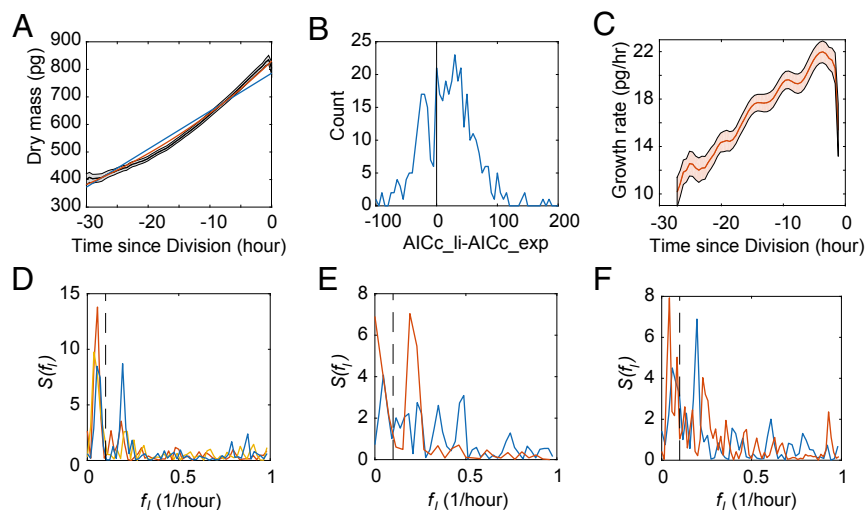
Fig. 4. Detection of the growth rate oscillations in adherent cells measured by ceQPM. (*A*) The mean trajectory (black) of the smoothed dry mass trajectories of HeLa cells aligned to cell division time, fitted by the linear (blue) or exponential (red) growth model. Data were collected from three independent replicative experiments, $n = 340$. The gray shaded regions indicate the 95% confidence intervals of the mean. (*B*) The histogram of the difference between the AICc of the linear (AICc_li) and exponential (AICc_exp) fit in HeLa cells. Better fits have the smaller AICc. The black vertical line indicates the difference equal to zero. (*C*) The mean trajectory of the smoothed growth rate trajectories of HeLa cells aligned to cell division time. The red shaded regions indicate the 95% confidence intervals of the mean. $n = 340$. (*D*) The periodogram of the mean trajectories of the detrended dry mass trajectories of HeLa cells aligned to cell division (blue), birth (red), and G1/S (yellow), respectively. $n = 340$. (*E*) The periodogram of the mean trajectories of the detrended dry mass trajectories of HeLa cells under thymidine treatment aligned to their chronological time (blue) or the first peak after G1/S transition (red). $n = 51$. (*F*) The periodogram of the mean trajectories of the detrended dry mass trajectories of HeLa cells under control condition (blue) or rapamycin treatment (red) aligned to cell division time. $n = 188$. The periodograms in *D*–*F* were estimated by the robust detection method as described in Ahdesmäki et al. (46). The black dashed lines indicate $f_{min} = 0.1/h$ used in the g′-statistic test.

the period of this peak is close to the average length of the cell cycle (26.2 h for HeLa cells), we designated it the "cell cycle" peak. The other peak at 0.193/h (5.2-h period) corresponds to the periodic bumps in the mean growth rate trajectory in Fig. 4*C*, which we designated as the "sub-cell cycle" peak. The "sub-cell cycle" peak is more dominant, its *P* value is 0.0014, meaning that the about 5-h periodicity is highly significant.

The "cell cycle" peak, however, can affect the significance of the "sub-cell cycle" peak. Especially when the "cell cycle" peak becomes the maximum peak in the periodogram, the robust detection method tests its significance rather than the "sub-cell cycle" peak. Since the "cell cycle" peak could be due to the imperfect detrending and we were more interested in the "sub-cell cycle" peak, we revised the question from "Is there is a significant peak in the periodogram?" to "Is there is a significant peak beyond the frequency f_{min}?," where the choice of f_{min} is chosen ad hoc to be higher than the "cell cycle" peak but lower than the "sub-cell cycle" peak. The period of the "cell cycle" peak can be longer or shorter than the cell cycle length, but is always longer than 10 h, we used $f_{min} = 0.1/h$ in most cases unless specified otherwise. As the robust detection method is insensitive to the choice of the *l* series, we can answer the new question within the same framework by modifying the g-statistic to

$$g'(f_l > f_{min}) = \frac{max_{i \leq l \leq 2N-1} S(f_l)}{\sum_{l=1}^{2N-1} S(f_l)},$$

where *i* is the smallest *l* of $f_l > f_{min}$. We validated the g′-statistic by investigating the false discovery rate (FDR) in random trajectories with Gaussian noise as well as mean trajectories of permutated single-cell trajectories. The FDR in both datasets was close to 5% when the *P* value was set to 0.05 (*SI Appendix, False Detection Rate (FDR) of g- and g′-Test*). According to the g′-statistic, the *P* value of the "sub-cell cycle" peak is less than 0.0002

(i.e., none of the 5,000 permutated trajectories has a larger g′), showing the striking clarity of the periodicity. In the following analysis, we alternatively used the g- or g′-statistic depending on the existence of "cell cycle" peaks, whose *P* values were defined as *p1* and *p2*, respectively.

Periodicity could have been induced by fluctuations in instrumentation, caused by temperature, light, line voltage, and so on, particularly if fluctuations coincided with built-in variation in the hardware. To investigate instrument fluctuation, we recorded the mass of fixed cells monitored for a long time. The fixed-cell data are not oscillatory (*p1* = 0.4334) (*SI Appendix*, Fig. S3 *G* and *H*). As proposed by Ahdesmäki et al. (46), we could use

$$g(f_l = f_x) = \frac{S(f_x)}{\sum_{l=1}^{2N-1} S(f_l)}, x \text{ belongs to } l$$

to test the significance at a specific frequency, f_x. The *P* value of $g(f_l = f_x)$ was defined as *p3*. According to this test, there is no significant peak near $f = 0.2/h$ (*p3* = 0.9999) in the periodogram of fixed cells. Hence, we conclude the ~5-h period in HeLa cells was not due to measurement oscillation caused by instrumental fluctuation.

We next tried to identify oscillations in individual cells. The g-statistic found 40 oscillatory cells out of 564 with *p1* smaller than 0.05 in the fixed-cell data, which occupied 7.1% of the population, whereas it found 106 oscillatory cells out of 340 in the live-cell data, which occupied 31.2% of the population (*SI Appendix*, Fig. S4 *A* and *B*). Since the oscillations of frequency smaller than 0.1/h could be due to imperfect detrending, we focused on the 62 oscillatory cells out of 340 of frequency larger than 0.1/h, whose percentage (18.2%) is still significantly larger than the 7.1% in fixed cells ($P = 7 \times 10^{-7}$ by Fisher's exact test). Their average oscillation frequency was 0.195/h, which was very close to the 0.193/h oscillation frequency of the mean trajectory of the whole population. The higher noise level of single-cell

Liu et al.

trajectories may have concealed the oscillation in the 68.8% of cells that did not meet $P < 0.05$ criteria. To probe whether these cells oscillated, we removed the 106 oscillatory cells from the dataset and took the mean trajectory of the remaining cells. The g'-statistic test of this mean trajectory showed oscillatory ($p2 = 0.0018$) (*SI Appendix*, Fig. S4C), suggesting that the growth rate oscillation in Fig. 4D was not caused by a subpopulation of cells but rather existed in the whole population. Similarly, we analyzed a dataset measured at the half acquisition time interval. Among the 143 full cell-cycle trajectories, we identified 32 oscillatory individuals of a frequency larger than 0.1/h (22.4% of the population). The average frequency is 0.212/h or 4.72 h in period (*SI Appendix*, Fig. S4 *D and E*), further confirming that the oscillatory behavior was not dependent on the experimental setting. It is worth noting that, the oscillation amplitude of the mean trajectory is 10 to 15% of the growth rate (Fig. 4C) or less than 0.5% of the average cell mass (3 pg vs. 600 pg), which is significantly smaller than the 2% measurement error of ceQPM in single-cell trajectories. When the measurement error was larger than the oscillation amplitude in single cells, the characteristic peak of the oscillation in the periodogram might be masked by random noise. However, if all cells oscillated at a similar frequency and were properly aligned by their oscillation phase, the random noise in the mean trajectory would be averaged out, leaving a distinct oscillation peak in the periodogram. This may explain why we did not detect oscillation at the single-cell level (but did in their mean trajectory) of the 68.8% cells. If it were the case, one would expect reducing the number of the constituent trajectories or aligning them to a different time could mask the oscillatory behavior in the mean trajectory. Indeed, we examined the mean trajectory of a single experiment, which happened to provide half of the data (170 cells). The traces distributed randomly within the experimental duration (*SI Appendix*, Fig. S4 *F–H*). When the trajectories were aligned to their division time, in its periodogram, the maximum peak of $f_l > 0.1$/h was at 0.196/h, consistent with the average of three experiments. Due to the smaller size of the dataset, there were more random peaks and $p2$ increased to 0.0840 (*SI Appendix*, Fig. S4I). When we aligned those trajectories to their chronological time rather than cell division, the ~0.2/h peak completely disappeared (*SI Appendix*, Fig. S4J). Instead, a distinct peak showed up at 0.983/h ($p1 < 0.0002$). During the experiment, we acquired phase images every 30 min and the fluorescent images every 1 h. The microscope spent a longer time on each FOV, scanning each position with both channels rather than just one channel; thus, the time interval in the trajectories was not even. However, we assumed it to be even in the data analysis, leading to the 1-h artificial oscillation. Our method was sensitive enough to pick up this subtle oscillation but indicated no significant peak around the 0.2/h frequency ($p3 = 0.9999$). This result further confirmed that the ~5-h-period oscillation in live cells was not introduced by environmental cues but was a reflection of intrinsic to growth rate regulation, and its phase was tightly coupled to cell division.

We next examined the oscillation phase relative to cell cycle events other than cell division. When we aligned all of the 340 trajectories of the three experiments to cell birth (which should be reasonably well correlated with cell division), the ~0.2/h peak in the periodogram was preserved ($f_c = 0.185$/h) but became less significant ($p2 = 0.0410$), whereas when we aligned the trajectories to the G1/S transition, the mean trajectory was no longer oscillatory ($p2 = 0.2849$) (Fig. 4D). We found similar results in RPE1 cells (*SI Appendix*, Fig. S4K). When the detrended cell mass trajectories of the RPE1 cells were aligned to cell division time, the mean trajectory was almost oscillatory ($p2 = 0.0794$) with two distinct peaks of $f_l > 0.1$/h The slightly higher peak was at $f_c = 0.324$/h, while the other peak was at 0.216/h, which was close to the ~0.2/h peak we observed in HeLa cells. When the trajectories were aligned to cell birth or G1/S, the mean

trajectory was not oscillatory with $p2$ of 0.7856 or 0.3647, respectively. Note that the cell number in the RPE1 dataset is smaller than in the HeLa dataset, and the two distinct peaks of similar height compromised the significance of periodicity in the test used currently, which was designed to detect a single oscillation frequency. Nonetheless, the main conclusion was the same as HeLa cells that the oscillation in the mean trajectory was much more pronounced when the cells were aligned to division than to birth or G1/S, suggesting a coupling between the growth rate oscillation and the cell division cycle. We further investigated HeLa cells under thymidine-induced cell cycle arrest. High levels of thymidine inhibit ribonucleotide reductase, inhibiting DNA synthesis and consequently arresting cells throughout S phase (51). Under this condition, we aligned all of the trajectories to the first peak after G1/S and found that the oscillation proceeded after the cells entered into S phase and arrested ($p2 < 0.0002$) (Fig. 4E). That the oscillation was maintained when the cell cycle was blocked implies that growth rate oscillation is independent of cell cycle progression. We note that cell growth continues when the cell cycle is arrested at S phase (*SI Appendix*, Fig. S4L). As growth rate is principally the net difference of protein synthesis and degradation, drugs inhibiting protein synthesis rate or activating protein degradation rate may be expected to perturb the oscillation. We therefore treated cells with rapamycin, which inhibits cell growth and activates degradation through the mTOR pathway (52). Such treatment made the mean trajectory less oscillatory compared to the normal growth condition for the same cell number ($p2 = 0.2487$ vs. $p2 = 0.0016$) with the f_c shifted from 0.1961/h to 0.2286/h (Fig. 4F).

All of these experiments above were done with adherent cells measured by ceQPM. We then asked whether oscillations in growth rate might be detected in suspension cells by the more accurate SMR method or whether it was not a phenomenon found in suspension cells. We are grateful for a large set of data of a mouse lymphoblastoid line, L1210, measured by Mu et al. (44). Since the SMR data were measured at such high accuracy and fine time resolution, we were readily able to reveal the periodicity in single cells. Similar to the QPM data, we first detrended the individual buoyant mass trajectories by the third-order polynomial, which fitted better than either of the linear or exponential growth models in all of the cells (*SI Appendix*, *Detrending the SMR Data*). The robust detection method found all of the 63 cells we analyzed individually were oscillatory with $p1$ less than 0.0002. Each cell only had one or two outstanding peaks in its periodogram. When we fitted individual trajectories with the generic cosine function,

$$yf_i = A cos\left(\frac{2\pi t_{i, i=1, ...,N}}{T} + \varphi\right),$$

where $t_{i, i=1, ...,N}$ is the time series, N is trajectory length, A is oscillation amplitude, T is oscillation period, and φ is the phase at $t_i = 0$ (Fig. 5 *A–F*), we could evaluate the goodness of fit by the adjusted residual sum of square (adj_RSS),

$$adj\_RSS = \frac{RSS}{A}, RSS = \sum_{i=1}^{N}(y_i - yf_i)^2,$$

where y_i is the observation and yf_i is the fitted result. Fig. 5G shows the distribution of adj_RSS of the 63 cells. We arbitrarily chose a cutoff threshold at $adj\_RSS = 50$ and only investigated the fitted results of the 56 out of 63 cells below the threshold. Note that the cells with adj_RSS above 50 were also oscillatory but with bigger variation (Fig. 5F). We found the average period was 3.6 h (Fig. 5H) and the average amplitude was 0.11 pg (about 0.2% of the averaged cell mass, or about 3% of the growth rate) (Fig. 5I). Unlike adherent cells, the oscillation phase in L1210
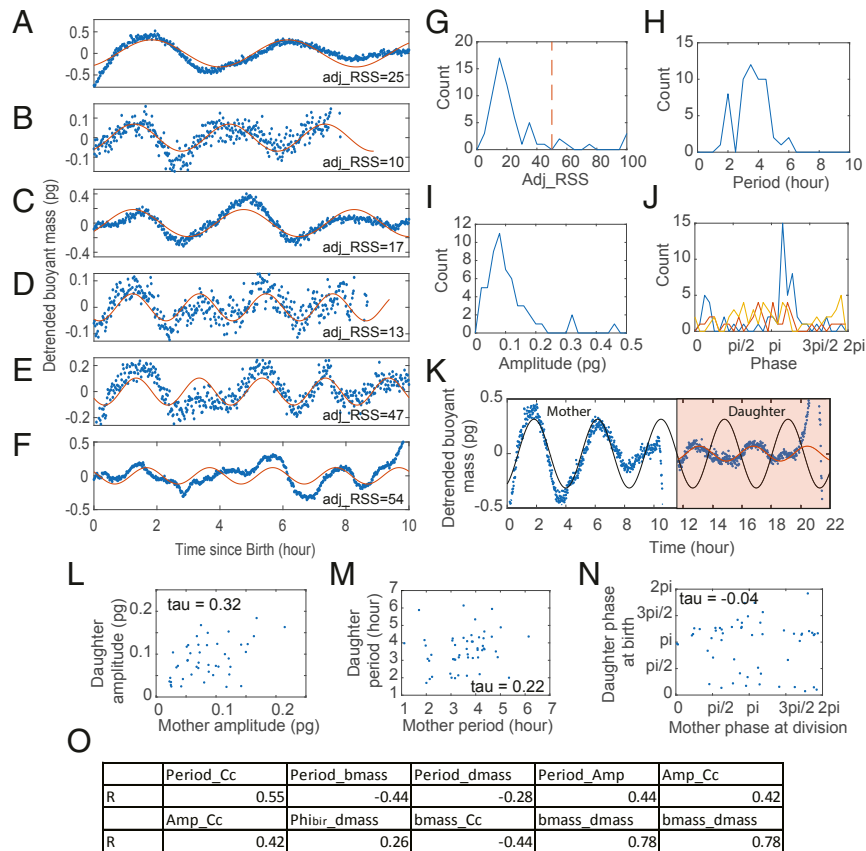
Fig. 5. Detection of growth rate oscillations in individual L1210 lymphoblast cells measured by SMR. (*A–F*) Examples of randomly selected detrended buoyant mass trajectories (blue dots). The solid red lines are the fitted cosine functions. adj_RSS indicates the goodness of fit. (*G–J*) The distributions of adj_RSS (*G*), period (*H*), amplitude (*I*), and phase at different cell cycle events (*J*) of the fitted cosine functions. The red dashed line in *G* indicates the arbitrary cutoff threshold; the distributions in *H–J* only include the 56 cells below that threshold. The blue, red, and yellow lines in *J* represent the oscillation phase at birth, G1/S, and division, respectively. Note that only 38 cells were measured with the fluorescent FUCCI marker and had identified G1/S timing. (*K*) The detrended buoyant mass trajectory of an example L1210 cell continued with the trajectory of one of its daughters (blue dot). The black and red lines are the fitted cosine functions of the mother and daughter cell, respectively. (*L–N*) The mother–daughter correlation of the oscillation amplitude (*L*), period (*M*), and phase (*N*). The correlation coefficients were calculated as Kendall's tau coefficient to avoid the effect of outliers. (*O*) The summary table of Pearson's correlations of *P* value smaller than 0.05. Cc denotes cell cycle length; bmass denotes birth mass; dmass denotes division mass; Amp denotes amplitude; Phi$_{bir}$ denotes the phase at birth.

	Period_Cc	Period_bmass	Period_dmass	Period_Amp	Amp_Cc
R	0.55	-0.44	-0.28	0.44	0.42
	Amp_Cc	Phi$_{bir}$_dmass	bmass_Cc	bmass_dmass	bmass_dmass
R	0.42	0.26	-0.44	0.78	0.78

cells was tightly coupled to cell birth but not so related to G1/S transition or cell division (Fig. 5*J*). As the SMR data traced the cell lineage for several generations, we also investigated the mother–daughter correlation of the oscillation properties (Fig. 5 *K–N*). We found positive correlations in oscillation amplitude and period among the mother and daughter cells (Fig. 5 *L* and *M*). However, the daughter cell does not inherit the phase from its mother, meaning the oscillation phase was reset at cell birth in each generation (Fig. 5 *K* and *N*). From this data we calculated the Pearson correlation between all of the measured variables. Fig. 5*O* summarized all of the correlations of *P* values smaller than 0.05. We found that period was strongly correlated with cell cycle length, and hence negatively correlated with cell size. Amplitude had a positive correlation with cell cycle length and period. The phase at birth was positively correlated with division mass.

In summary, we identified the growth rate oscillations in two adherent cell lines, HeLa and RPE1, and one suspension cell line, L1210, which had roughly similar periods (3.1 to 5.2 h) and comparable amplitudes (0.2 to 0.5% of the averaged cell size, or 3 to 15% of the growth rate). The oscillations were measured by the two most accurate but totally distinct methods at different time resolutions, confirming the periodicity is real and virtually impossible to have been caused by experimental or analytical artifacts.

Discussion

How cell growth and cell division are coordinated has been a persistent but very difficult problem. The difficulty arises primarily from the challenge of making accurate measurements of cell mass over time in single cells. The most commonly used and thoroughly studied mammalian cells are cells attached to plastic or glass. They have many experimental advantages for some technologies but fail for others. QPM has become the optimal method to measure cell mass in adherent cells (18, 25, 33, 53, 54). Yet, the sensitivity of QPM has not been sufficient to decide among various models for growth, such as whether proliferating cells acquire mass in a linear manner (independent of cell mass) or an exponential manner (proportional to cell mass). We have made several computational innovations in QPM, producing an improved technique, which we call computationally enhanced ceQPM. It improves measurement accuracy by more than twofold. ceQPM also improves the stability and repeatability of the measurement, which is critical in comparing experiments. ceQPM permitted the use of low-magnification lenses, which cover a much larger field and measure more cells per unit time. Furthermore, advanced data acquisition throughput increases the statistical power of the experiments, for example allowing us to demonstrate new biological features that can be evaluated by

Liu et al.

www.manaraa.com

statistical tests. The automated cell segmentation and tracking algorithms facilitate the processing of large datasets. Both the experimental and analytical systems can be incorporated into broad applications to phenomena of cell size and cell growth. We have used this improved method to explore the growth of two adherent cell lines, HeLa and RPE1 cells. Both cell lines more closely fit an exponential, rather than a linear, model of growth. Yet, neither the exponential nor the linear model fits all of the cells; the exponential model fits better in about two-thirds of the population.

When we looked carefully at the growth curves, we found clear hints of oscillatory behavior. On deeper analysis, there was a 3.1- to 5.2-h oscillation in growth rate in HeLa and RPE1 cells, which is coupled to cell division time but unrelated to the G1/S transition of the cell cycle. Note that although later pooled and synchronized in silico, these cells were measured from asynchronous populations in different experiments so that the experimental time bears no relationship to real-time and the individual members of the population can be expected to be scrambled with respect to time in each experiment. It rules out the possibility that the periodicities arose from environmental fluctuation (such as temperature or line voltage) or some collective signal among the cells in the well. We also observed a growth rate oscillation of comparable period and amplitude in a suspension cell line, L1210 lymphoblast, measured by SMR. The SMR, having at least 100 times better accuracy and 25 times higher time resolution than the ceQPM measurements, detected the periodicity in all of the individual cells tested. Ultradian oscillations in protein synthesis has been reported several times in drug-induced synchronous cultures (55–58), and the periodic cell size changes or protein production rate caused by metabolic oscillation was also discovered in individual budding yeast cells (59, 60). However, the idea of endogenous growth rate oscillation has never been widely considered due to the lack of convincing experimental evidence. In this study, we discovered the oscillations in unperturbed cells of two adherent cell lines measured by ceQPM and one suspension cell line measured by SMR, suggesting that periodicity may be a general property of growth dynamics and may even exist in nondividing cells.

At this point, we do not know the underlying mechanisms of the growth rate oscillations. However, the limited pharmacological perturbations provide some hints. The blockage of the nuclear division cycle with thymidine did not arrest the oscillation, suggesting that the oscillation is independent of cell cycle progression. The partial inhibition of growth with rapamycin weakened the periodicity and shortened the period from 5.1 h to 4.4 h, suggesting a plausible linkage to the mTOR signaling pathway. The mTOR pathway up-regulates the translational machinery through the phosphorylation of p70^{s6k} kinase and 4E-BP1, thus activating the translation initiation. It also down-regulates the degradative process by inhibiting autophagy and lysosome biogenesis (2, 4). Both regulation of the synthesis and degradation processes could cause growth rate oscillation. Methods for measuring the protein synthesis and degradation rates at the single-cell level would greatly help to dissect the underlying control mechanisms. Furthermore, the study of the correlations between the oscillation parameters (amplitude, period, and phase) and the cell properties (cell mass, cell cycle length, etc.) could also provide a better understanding of the oscillation. Another possible cause of the oscillation would be a circadian rhythm, which is known to be coupled to many periodic behaviors in the cell (58, 61, 62). However, until we understand the growth rate oscillation in molecular terms, we will not know whether these two rhythms are connected.

Although the growth rate oscillation is autonomous, its phase is coupled to cell division in HeLa and RPE1 and to birth in L1210 cells, which suggests possible mutual entrainment between the growth rate oscillation and a specific cell cycle event. The growth rate oscillation may serve as a gate to mitosis by controlling the

availability of metabolites and cellular energy level. On the other hand, mitosis is the most dramatic event in the cell cycle, perturbing cell architecture, nuclear function, and secretion (63). During the central events of mitosis, RNA and protein synthesis pauses, cellular adenosine 5′-triphosphate (ATP) is depleted, the cell volume swells, and cell density decreases (14, 15, 21, 64). All of these might reinforce or reset the oscillation, as the cells restore their original state. Investigating the coupling between cell growth and cell cycle oscillations could provide novel understandings of both (59, 65–68). The coordination between the two is critical for cell size regulation and may shed light on the cause of heterogeneous drug response among isogenic cells in cancer therapy.

At this time, we can only speculate as to why control takes the form of an oscillation. In engineering and in biological circuits, oscillations are often caused by negative feedback with a substantial time delay and are property of systems that maintain homeostasis (69). The growth rate oscillation could serve such a function or simply be a by-product of other oscillations. In investigating the "purpose" of oscillations, it is often hard to establish causality, because many cellular processes may depend on synthesis and degradation. Nevertheless, one possible role of the oscillation could be to maintain the cell size and growth rate. The negative feedback between cell size and growth rate in proliferating cells could bring the growth rate back to a targeted level after it has been perturbed by transient signals or random drifts (23, 34, 67). Protein synthesis and degradation rates may be in better balance in nonproliferating cells for use in stabilizing size (70). The growth rate oscillation might also function in cell mass density homeostasis. The variability in cell mass density is much smaller than cell mass and seems to be under tight control (71). Cell density might be expected to affect cell mass growth rate through changing the synthesis and degradation rates as affected by molecular crowding or dilution (72, 73). In turn, cell mass growth rate might feedback on cell density, as the independent regulation of cell mass and volume are often out of phase (10, 74). Finally, other homeostatic circuits could regulate such things as the nuclear-cytoplasmic ratio and link to the growth rate oscillation (75). A whole new set of genetic and pharmacological experiments should now be possible that depend on accurate quantitative analysis of mass and growth rate. These experiments should help us understand various types oscillations and transients in the cell.

Materials and Methods

Cell Culture. HeLa Geminin-GFP and RPE1 Geminin-GFP cells were generated and single clones were isolated and grown in our laboratory (12). Cells were kept in Dulbecco's modified Eagle's medium (DMEM) (11965; Thermo Fisher Scientific) supplemented with 10% fetal bovine serum (FBS) (16000044; Thermo Fisher Scientific), 1% penicillin/streptomycin (10,000 U/mL, 15140122; Thermo Fisher Scientific), 10 mM sodium pyruvate (100 mM, 11360070; Thermo Fisher Scientific), and 25 mM Hepes (1 M, 15630080; Thermo Fisher Scientific) and incubated at 37 °C with 5% CO_2. Rapamycin used to inhibit mTOR activity was purchased from LC Laboratories (R-5000). Thymidine to arrest cell cycle was purchased from Sigma-Aldrich (T1895).

Microscope Setup. The SID4BIO camera (Phasics) was integrated into a Nikon Eclipse Ti microscope through a C-mount. For QPM imaging, we used a halogen lamp as the transmitted light source. A Nikon LWD numerical aperture (N.A.) 0.52 condenser was used with the aperture diaphragm minimized. A C-HGFI mercury lamp was used for fluorescence illumination. A Nikon TI-S-ER motorized stage was used to position the sample with the moving speed of 2.5 mm/s in the X–Y direction (accuracy 0.1 μm). A Nikon Perfect Focus System (PFS) was used for maintaining the focus. An Endow GFP/EGFP filter set (Chroma 41017) was used to take the Geminin-GFP image. We used three objective lenses as indicated in this study, one Nikon Plan Flour 10× N.A. 0.3 PFS dry, one Nikon Plan Apo 20× N.A. 0.75 PFS dry, and one Nikon Plan Apo 40× N.A. 0.95 PFS dry. NIS-Elements AR ver. 4.13.0.1 software with the WellPlate plugin was used to acquire images. A homemade incubation chamber was used to maintain a constant environment of 36 °C and 5% CO_2.

www.manaraa.com

Quantification of QPM Measurement Errors. To quantify the OPD noise of the blank sample, we performed all of the measurements as described on the blank six-well glass-bottom plates filled by phosphate-buffered saline (PBS) (21-040-CV; Corning) and covered with mineral oil (M8410; Sigma-Aldrich) at 10× magnification.

Fixed cells were used to quantify the dry mass and growth rate measurement error. For sample preparation, HeLa cells were seeded in six-well glass-bottom plates (P06-1.5H-N; Cellvis) at 3,500 cells per cm² overnight then fixed in 0.2% glutaraldehyde (50 wt % in water; 340855; Sigma-Aldrich) for 10 min at room temperature. Then the fixed cells were immersed in PBS and topped with mineral oil.

In the experiments to quantify the dry mass measurement error, cells were imaged every 5 min for 2 h. At 10× magnification, an area of 8 × 8 FOVs in the well center was scanned, with the X–Y step distance as one-fifth of the FOV. At 20×, an area of 15 × 15 FOVs was scanned, with one-fifth of the FOV as the step distance. At 40×, 60 cells were chosen manually; each was imaged in four FOVs with the cell at a different corner. The temporal error was quantified as the SD of the time series of each cell divided by the mean mass of the cell. To quantify the net spatial error, we averaged the dry mass measurements through the time series first to eliminate the error caused by the temporal variation then took the SD divided by the mean of each cell at different positions as the spatial error. The temporal and spatial combined error was the SD divided by the mean of each cell at different positions without averaging by time series.

Long-Term Live-Cell Imaging under QPM. The six-well glass-bottom plates were treated by Plasma Etcher 500-II (Technics West Inc.) at 75 mTorr, 110 W, for 1 min then coated by 50 μg/mL fibronectin (F1141; Sigma-Aldrich) overnight. Cells were seeded on the precoated plates at 2,000 cells per cm² 3 h prior to the experiments in the medium of DMEM without phenol red (21063; Thermo Fisher Scientific) supplemented with 10% FBS, 1% penicillin/streptomycin, and 10 mM sodium pyruvate and topped with mineral oil. All of the experiments were done at 10× magnification. The phase images were acquired every 30 min, and the fluorescent images were acquired every 1 h, at 36 °C by the SID4BIO camera. The HeLa cells in normal growth condition or with thymidine were monitored for 40 to 48 h. The RPE cells were monitored for 36 to 45 h. The HeLa cells with rapamycin were monitored for 70 to 72 h. The drugs were added just before the time-lapse movie. The position of the FOVs was generated by a custom-developed GUI in MATLAB (MathWorks), which ensured that the FOVs were within the center 10% area of the well and were evenly spaced. Seventy-two FOVs were imaged in each well. The fixed cells used to analyze instrumental fluctuation were imaged every 30 min for 27 h. The 15-min-interval experiment was measured similarly to the 30-min-interval experiments, but at higher acquisition frequency and without fluorescence detection. In the experiment, live HeLa cells were monitored for 48 h.

Fibronectin Immunostaining. HeLa cells were seeded and monitored by QPM for 24 h, as described in the previous section. The mineral oil was gently removed by aspiration. Cells were then permeabilized with the permeabilization buffer (76) and fixed with 4% paraformaldehyde (RT 157-8; Electron Microscopy Sciences). After blocking with 2% BSA for 1 h, cells were incubated with or without the anti-fibronectin primary antibody (1:100, ab2413; Abcam) overnight at 4 °C then incubated with the goat anti-rabbit IgG (H+L) secondary antibody Alexa Fluor 568 (1:1,000, A-11011; Thermo Fisher Scientific) for 1 h at room temperature. Finally, cells were stained with 250 ng/mL Alexa Fluor 647 NHS ester (A20006; Thermo Fisher Scientific) and 2 μM DAPI (4, 6- diamidino-2- phenylindole) (D8417; Sigma-Aldrich) for 1 h at room temperature and imaged by the ORCA-ER camera (Hamamatsu) at 10× magnification.

QPM Image Analysis and Data Processing. We developed a custom GUI to evaluate the performance of the synthetic reference and parameters for segmentation. All of the image processing pipeline (generating the reference wavefront, applying the reference, background subtraction, cell segmentation, and cell tracking) was conducted on a high-performance compute cluster by custom-written codes in MATLAB. To get the most accurate growth rate measurement, we cleaned up all of the data points of contact or rounded cells. This data filtering process created gaps in the cell tracking trajectories. We discarded all of the trajectories with any single gap longer than 3 h or total gap longer than 6 h. The filtering process also removed the data immediately after birth and before mitosis. Thus, we considered any trajectory that begins less than 3 h after birth and ends less than 1 h before mitosis as a trajectory of the full cell cycle. The gaps in the trajectories were filled by linear interpolation. For HeLa cells arrested by thymidine, any trajectory longer than 12 h and with an identified G1/S transition was adopted.

For each condition, the trajectories were collected from more than three independent experiments except for the thymidine treatment and the 15-min-interval experiment, which were done only once.

To get the single-cell growth rate trajectory, we applied cubic spline smoothing (the csaps function in MATLAB) on the dry mass trajectories at the smoothing parameter $P = 0.00002$ and then fitted the linear growth rate in a 3-h sliding window to further reduce noise. The same processing was applied to fixed-cell data after leveling to demonstrate their effect on the power spectrum.

The dry mass trajectories were fitted by the linear, exponential, or second-order polynomial functions using linear (for the linear function) or nonlinear least squares (for the exponential and second-order polynomial functions) fit with bisquare weighting to eliminate the impact of outliers. The goodness of fit was estimated by the AICc (45):

$$AICc = N\log\left(\frac{RSS}{N}\right) + 2M + \frac{2M(M-1)}{N-M-1},$$

where RSS is the residual sum of squares of the fit, N is the number of data points, and M is the number of parameters in the function.

The dry mass, growth rate, or detrended dry mass trajectories were aligned and averaged as indicated. When the trajectories were aligned to birth, G1/S, or chronological time, the last 2 h before division was trimmed to avoid the impact of the abrupt mitotic dip. In the thymidine-treated data, since the detrended dry mass trajectory was too noisy, the first peak after G1/S was identified by the smoothed growth rate trajectory. Since the trajectory length varied a lot among cells, the mean trajectory only included data points of the average of more than 50 trajectories except for the dataset of thymidine treatment, where the threshold was reduced to 25 due to the low cell number. The 95% confidence intervals of the mean trajectory were calculated as $[\bar{x} + t_{0.025,\,n-1}SEM, \bar{x} + t_{0.975,\,n-1}SEM]$, where n is the trajectory number, SEM is the SEM, $\sigma_{\bar{x}} = \frac{\sigma}{\sqrt{n}}$, and $t_{0.025,\,n-1}$ and $t_{0.975,\,n-1}$ are the t-scores at 2.5% and 97.5% tails with degree of freedom equal to $n-1$.

SMR Data Analysis. The L1210 data were adopted from the L1210 FUCCI control dataset measured by the small-channel SMR in Mu et al. (44). A total number of 63 cells measured in nine independent experiments were analyzed. As the time interval of the SMR data were irregular with a mean at 1.1 min, we first linear-interpolated the data at a fixed time interval of 1.2 min. The buoyant mass trajectories were fitted by the linear, exponential, and polynomial functions. The goodness of fit of different functions was compared by the AIC (77), $AIC = N\log\left(\frac{RSS}{N}\right) + 2M$. All of the trajectories were detrended by the third-order polynomial in further analysis. The robust periodogram of the detrended trajectories was estimated and the periodicity was tested by the robust detection method. The detrended trajectories were fitted by the generic cosine function, $A\cos\left(\frac{2\pi t_{i,\,i=1,...,N}}{T} + \varphi\right)$, using the nonlinear least-square fit. The last 2 h before division was trimmed before fitting to remove the mitotic dip. The frequency of the maximum peak in the periodogram was adopted to calculate the initial value of T for the fitting.

Periodogram and Robust Periodicity Detection. The robust periodogram was estimated by the correlogram as described in Ahdesmäki et al. (46). In the cases of QPM trajectories aligned to cell division, the last 1 h before division was trimmed off from the mean trajectory to avoid the dramatic impact of the mitotic dip on the periodogram. The last 2 h of the SMR trajectory aligned to mitotic dip were trimmed off for the same reason. For the thymidine-treated cells aligned to the first peak after G1/S, the mean trajectory after the first dip after G1/S was used to estimate the periodogram of the arrested S phase. All of the significances were assigned by the permutation method. The implementation was realized by the MATLAB source code provided in Ahdesmäki et al. (46) with slight modification. All of the results of the statistical tests are summarized in *SI Appendix*, Table S2.

Data Availability. All of the cell mass trajectories and their cell cycle events, measured by the QPM and used in the analyses, are summarized in an Excel spreadsheet and are available as Dataset S1. Other less-complete datasets are also available upon request. The ceQPM software is available at https://www.mathworks.com/matlabcentral/fileexchange/75387-computationally-enhanced-quantitative-phase-microscopy.

www.manaraa.com

1. I. Conlon, M. Raff, Size control in animal development. *Cell* **96**, 235–244 (1999).

2. T. Schmelzle, M. N. Hall, TOR, a central controller of cell growth. *Cell* **103**, 253–262 (2000).

3. S. Sulić, L. Panić, I. Dikić, S. Volarević, Deregulation of cell growth and malignant transformation. *Croat. Med. J.* **46**, 622–638 (2005).

4. M. Laplante, D. M. Sabatini, mTOR signaling in growth control and disease. *Cell* **149**, 274–293 (2012).

5. S. C. Kozma, G. Thomas, Regulation of cell size in growth, development and human disease: PI3K, PKB and S6K. *BioEssays* **24**, 65–71 (2002).

6. D. A. Guertin, D. M. Sabatini, "Cell growth" in *The Molecular Basis of Cancer*, J. Mendelsohn, P. M. Howley, M. A. Israel, J. W. Gray, C. R. Thompson, Eds. (Elsevier, ed. 4, 2014), pp. 179–190.

7. I. Conlon, M. Raff, Differences in the way a mammalian cell and yeast cells coordinate cell growth and cell-cycle progression. *J. Biol.* **2**, 7 (2003).

8. J. M. Mitchison, Growth during the cell cycle. *Int. Rev. Cytol.* **226**, 165–258 (2003).

9. S. Cooper, Rethinking synchronization of mammalian cells for cell cycle analysis. *Cell. Mol. Life Sci.* **60**, 1099–1106 (2003).

10. G. E. Neurohr *et al.*, Excessive cell growth causes cytoplasm dilution and contributes to senescence. *Cell* **176**, 1083–1097.e18 (2019).

11. Y. Sung *et al.*, Size homeostasis in adherent cells studied by synthetic phase micros-copy. *Proc. Natl. Acad. Sci. U.S.A.* **110**, 16687–16692 (2013).

12. R. Kafri *et al.*, Dynamics extracted from fixed cells reveal feedback linking cell growth to cell cycle. *Nature* **494**, 480–483 (2013).

13. A. Tzur, R. Kafri, V. S. LeBleu, G. Lahav, M. W. Kirschner, Cell growth and size ho-meostasis in proliferating animal cells. *Science* **325**, 167–171 (2009).

14. E. Zlotek-Zlotkiewicz, S. Monnier, G. Cappello, M. Le Berre, M. Piel, Optical volume and mass measurements show that mammalian cells swell during mitosis. *J. Cell Biol.* **211**, 765–774 (2015).

15. S. Son *et al.*, Resonant microchannel volume and mass measurements show that suspended cells swell during mitosis. *J. Cell Biol.* **211**, 757–763 (2015).

16. K. L. Cooper *et al.*, Multiple phases of chondrocyte enlargement underlie differences in skeletal proportions. *Nature* **495**, 375–378 (2013).

17. C. Cadart, L. Venkova, P. Recho, M. C. Lagomarsino, M. Piel, The physics of cell-size regulation across timescales. *Nat. Phys.* **15**, 993–1004 (2019).

18. T. A. Zangle, M. A. Teitell, Live-cell mass profiling: An emerging approach in quan-titative biophysics. *Nat. Methods* **11**, 1221–1228 (2014).

19. M. Godin *et al.*, Using buoyant mass to measure the growth of single cells. *Nat. Methods* **7**, 387–390 (2010).

20. S. Son *et al.*, Direct observation of mammalian cell growth and size regulation. *Nat. Methods* **9**, 910–912 (2012).

21. T. P. Miettinen, J. H. Kang, L. F. Yang, S. R. Manalis, Mammalian cell growth dynamics in mitosis. *eLife* **8**, 1–29 (2019).

22. N. Cermak *et al.*, High-throughput measurement of single-cell growth rates using serial microfluidic mass sensor arrays. *Nat. Biotechnol.* **34**, 1052–1059 (2016).

23. M. B. Ginzberg *et al.*, Cell size sensing in animal cells coordinates anabolic growth rates and cell cycle progression to maintain cell size uniformity. *eLife* **7**, 123851 (2018).

24. D. F. Berenson, E. Zatulovskiy, S. Xie, J. M. Skotheim, Constitutive expression of a fluorescent protein reports the size of live human cells. *Mol. Biol. Cell* **30**, 2943–3012 (2019).

25. J. Reed *et al.*, Rapid, massively parallel single-cell drug response measurements via live cell interferometry. *Biophys. J.* **101**, 1025–1031 (2011).

26. S. Aknoun *et al.*, Living cell dry mass measurement using quantitative phase imaging with quadriwave lateral shearing interferometry: An accuracy and sensitivity discus-sion. *J. Biomed. Opt.* **20**, 126009 (2015).

27. C. Allier *et al.*, Quantitative phase imaging of adherent mammalian cells: A com-parative study. *Biomed. Opt. Express* **10**, 2768–2783 (2019).

28. P. Bon, G. Maucort, B. Wattellier, S. Monneret, Quadriwave lateral shearing inter-ferometry for quantitative phase microscopy of living cells. *Opt. Express* **17**, 13080–13094 (2009).

29. Z. Wang, "Spatial light interference microscopy (SLIM)" in *IEEE Photonic Society 24th Annual Meeting PHO 2011*, (IEEE, 2011), Vol. 19, p. 797.

30. J. Marrison, L. Räty, P. Marriott, P. O'Toole, Ptychography–A label free, high-contrast imaging technique for live cells using quantitative phase information. *Sci. Rep.* **3**, 2369 (2013).

31. P. Marquet *et al.*, Digital holographic microscopy: A noninvasive contrast imaging technique allowing quantitative visualization of living cells with subwavelength axial accuracy. *Opt. Lett.* **30**, 468–470 (2005).

32. P. Bon, J. Savatier, M. Merlin, B. Wattellier, S. Monneret, Optical detection and measurement of living cell morphometric features with single-shot quantitative phase microscopy. *J. Biomed. Opt.* **17**, 076004 (2012).

33. M. Mir *et al.*, Optical measurement of cycle-dependent cell growth. *Proc. Natl. Acad. Sci. U.S.A.* **108**, 13124–13129 (2011).

34. C. Cadart *et al.*, Size control in mammalian cells involves modulation of both growth rate and cell cycle duration. *Nat. Commun.* **9**, 3275 (2018).

35. D. Martínez-Martín *et al.*, Inertial picobalance reveals fast mass fluctuations in mammalian cells. *Nature* **550**, 500–505 (2017).

36. R. Barer, Interference microscopy and mass determination. *Nature* **169**, 366–367 (1952).

37. R. Barer, S. Joseph, Refractometry of living cells: Part 1. Basic principles. *Q. J. Microsc. Sci.* **95**, 399–423 (1954).

38. J. C. Chanteloup, Multiple-wave lateral shearing interferometry for wave-front sensing. *Appl. Opt.* **44**, 1559–1571 (2005).

39. M. R. Arnison, K. G. Larkin, C. J. R. Sheppard, N. I. Smith, C. J. Cogswell, Linear phase imaging using differential interference contrast microscopy. *J. Microsc.* **214**, 7–12 (2004).

40. G. Goldstein, K. Creath, Quantitative phase microscopy: Automated background leveling techniques and smart temporal phase unwrapping. *Appl. Opt.* **54**, 5175–5185 (2015).

41. G. Wahba, *Spline Models for Observational Data*, (Society for Industrial and Applied Mathematics, 1990).

42. P. Soille, *Morphological Image Analysis-Principles and Applications*, (Springer, ed. 2, 2004).

43. A. Sakaue-Sawano *et al.*, Visualizing spatiotemporal dynamics of multicellular cell-cycle progression. *Cell* **132**, 487–498 (2008).

44. L. Mu *et al.*, Mass measurements during lymphocytic leukemia cell polyploidization decouple cell cycle- and cell size-dependent growth. *Proc. Natl. Acad. Sci. U.S.A.* **117**, 15659–15665 (2020).

45. K. P. Burnham, D. R. Anderson, *Model Selection and Inference: A Practical Informa-tion-Theoretic Approach*, (Springer, 2001).

46. M. Ahdesmäki, H. Lähdesmäki, R. Pearson, H. Huttunen, O. Yli-Harja, Robust detec-tion of periodic time series measured from biological systems. *BMC Bioinformatics* **6**, 117 (2005).

47. J. Ireland, M. S. Marsh, T. A. Kucera, C. A. Young, Automated detection of oscillating regions in the solar atmosphere. *Sol. Phys.* **264**, 403–431 (2010).

48. N. E. Phillips, C. Manning, N. Papalopulu, M. Rattray, Identifying stochastic oscillations in single-cell live imaging time series using Gaussian processes. *PLOS Comput. Biol.* **13**, e1005479 (2017).

49. Y. Tanouchi *et al.*, A noisy linear map underlies oscillations in cell size and gene ex-pression in bacteria. *Nature* **523**, 357–360 (2015).

50. S. Wichert, K. Fokianos, K. Strimmer, Identifying periodically expressed transcripts in microarray time series data. *Bioinformatics* **20**, 5–20 (2004).

51. Z. Darzynkiewicz, H. D. Halicaka, H. Zhao, M. Podhorecka, "Cell synchronization by inhibitors of DNA replication induces replication stress and DNA damage response: Analysis by flow cytometry" in *Cell Cycle Synchronization: Methods and Protocols*, G. Banfalvi, Ed. (Humana Press, ed. 1, 2011), pp. 85–96.

52. S. Wullschleger, R. Loewith, M. N. Hall, TOR signaling in growth and metabolism. *Cell* **124**, 471–484 (2006).

53. G. Popescu *et al.*, Optical imaging of cell mass and growth dynamics. *Am. J. Physiol. Cell Physiol.* **295**, C538–C544 (2008).

54. S. Sridharan, M. Mir, G. Popescu, Simultaneous optical measurements of cell motility and growth. *Biomed. Opt. Express* **2**, 2815–2820 (2011).

55. R. R. Klevecz, Temporal order in mammalian cells. I. The periodic synthesis of lactate dehydrogenase in the cell cycle. *J. Cell Biol.* **43**, 207–219 (1969).

56. R. R. Klevecz, F. H. Ruddle, Cyclic changes in enzyme activity in synchronized mam-malian cell cultures. *Science* **159**, 634–636 (1968).

57. D. Lloyd, R. K. Poole, S. W. Edwards, *The Cell Division Cycle: Temporal Organi-sation and Control of Cellular Growth and Reproduction*, (Academic Press, London, 1982).

58. D. Lloyd, S. W. Edwards, J. C. Fry, Temperature-compensated oscillations in respiration and cellular protein content in synchronous cultures of Acanthamoeba castellanii. *Proc. Natl. Acad. Sci. U.S.A.* **79**, 3785–3788 (1982).

59. A. Papagiannakis, B. Niebel, E. C. Wit, M. Heinemann, Autonomous meta-bolic oscillations robustly gate the early and late cell cycle. *Mol. Cell* **65**, 285–295 (2017).

60. A. Litsios *et al.*, Differential scaling between G1 protein production and cell size dy-namics promotes commitment to the cell division cycle in budding yeast. *Nat. Cell Biol.* **21**, 1382–1392 (2019).

61. J. Zámborszky, C. I. Hong, A. Csikász Nagy, Computational analysis of mammalian cell division gated by a circadian clock: Quantized cell cycles and cell size control. *J. Biol. Rhythms* **22**, 542–553 (2007).

62. J. Mellor, The molecular basis of metabolic cycles and their relationship to circadian rhythms. *Nat. Struct. Mol. Biol.* **23**, 1035–1044 (2016).

63. G. M. Cooper, "The nucleus during mitosis" in *The Cell: A Molecular Approach*, (Si-nauer Associates, Sunderland, MA, ed. 2, 2000), https://www.ncbi.nlm.nih.gov/books/NBK9890/.

64. J. H. Kang *et al.*, Time-dynamics of mitochondrial membrane potential reveal an inhibition of ATP synthesis in mitosis. bioRxiv:10.1101/772244 (18 September 2019).

www.manaraa.com

65. E. Ahn, P. Kumar, D. Mukha, A. Tzur, T. Shlomi, Temporal fluxomics reveals oscillations in TCA cycle flux throughout the mammalian cell cycle. *Mol. Syst. Biol.* **13**, 953 (2017).

66. T. P. Miettinen *et al.*, Identification of transcriptional and metabolic programs related to mammalian cell size. *Curr. Biol.* **24**, 598–608 (2014).

67. M. Björklund, Cell size homeostasis: Metabolic control of growth and cell division. *Biochim. Biophys. Acta Mol. Cell Res.* **1866**, 409–417 (2019).

68. Y. Arata, H. Takagi, Quantitative studies for cell-division cycle control. *Front. Physiol.* **10**, 1022 (2019).

69. L. Glass, A. Beuter, D. Larocque, Time delays, oscillations, and chaos in physiological control systems. *Math. Biosci.* **90**, 111–125 (1988).

70. A. C. Lloyd, The regulation of cell size. *Cell* **154**, 1194–1205 (2013).

71. G. E. Neurohr, A. Amon, Relevance and regulation of cell density. *Trends Cell Biol.* **30**, 213–225 (2020).

72. S. Klumpp, M. Scott, S. Pedersen, T. Hwa, Molecular crowding limits translation and cell growth. *Proc. Natl. Acad. Sci. U.S.A.* **110**, 16754–16759 (2013).

73. S. Pfeffer *et al.*, mTORC1 controls phase separation and the biophysical properties of the cytoplasm by tuning article mTORC1 controls phase separation and the biophysical properties of the cytoplasm by tuning crowding. *Cell* **174**, 338–349.e20 (2018).

74. B. D. Knapp *et al.*, Decoupling of rates of protein synthesis from cell expansion leads to supergrowth. *Cell Syst.* **9**, 434–445.e6 (2019).

75. H. Cantwell, P. Nurse, Unravelling nuclear size control. *Curr. Genet.* **65**, 1281–1285 (2019).

76. A. Das, A. Kapoor, G. D. Mehta, S. K. Ghosh, S. Sen, Mutagenesis extracellular matrix density regulates extracellular proteolysis via modulation of cellular contractility. *J. Carcinogene. Mutagene.*, 10.4172/2157-2518.S13-003 (2013).

77. H. Akaike, "Information theory and an extension of the maximum likelihood principle" in *Proceedings of the 2nd International Symposium on Information Theory*, (Akadémiai Kiado, 1973), pp. 267–281.

www.manaraa.com